electronics

MDPI

Article

Metamaterial-Based Series-Fed Antenna with a High Gain and Wideband Performance for Millimeter-Wave Spectrum Applications

Bashar A. F. Esmail [1,2], Slawomir Koziel [1,3] and Dustin Isleifson [2,*]

[1] Department of Engineering, Reykjavik University, 102 Reykjavík, Iceland; bashar.esmail@umanitoba.ca (B.A.F.E.); koziel@ru.is (S.K.)
[2] Department of Electrical & Computer Engineering, University of Manitoba, Winnipeg, MB R3T 5V6, Canada
[3] Faculty of Electronics, Telecommunications and Informatics, Gdansk University of Technology, 80-233 Gdansk, Poland
* Correspondence: dustin.isleifson@umanitoba.ca

Abstract: This paper presents a high-gain, wideband series-fed antenna designed for 5G millimeter-wave (MMW) applications. The structure employs a substrate-integrated-waveguide (SIW)-based power splitter and metamaterials (MMs). The power divider functions effectively at 27.5 GHz, exhibiting an impedance bandwidth from 26.9 to 28.6 GHz. The series-fed dipole is assembled on the SIW-based power splitter, incorporating four dipoles with varying lengths and spacing. The dipoles are connected in series on both sides, running in parallel through a microstrip line. Effectively combining the resonances of the series-fed dipoles and the SIW results in a broad impedance bandwidth, ranging from 26.9 GHz to 34.75 GHz. The design has a gain extending from 9 to 10.5 dBi within the operating bandwidth. To improve gain performance without a substantial increase in antenna size, 11 × 6 MM unit cells were positioned in front of the antenna. As a result, the proposed antenna achieves a maximum gain of 14.1 dBi at 30.5 GHz while maintaining an operational bandwidth of 7.85 GHz. Additionally, due to the arrangement of the two MM-based series-fed dipoles, the antenna exhibits symmetrical dual-beam E-plane radiation at ±20° and 28 GHz in the end-fire direction. The developed system was experimentally validated and an excellent agreement between the simulated and measured data was demonstrated.

Keywords: 5G; high-gain antenna; metamaterials; MMW; SIW

Citation: Esmail, B.A.F.; Koziel, S.; Isleifson, D. Metamaterial-Based Series-Fed Antenna with a High Gain and Wideband Performance for Millimeter-Wave Spectrum Applications. *Electronics* **2023**, *12*, 4836. https://doi.org/10.3390/electronics12234836

Received: 27 October 2023
Revised: 22 November 2023
Accepted: 28 November 2023
Published: 30 November 2023

1. Introduction

The predominant motivation for the advancement of fifth-generation (5G) technology stems from the rising need for expansive bandwidth and elevated data rates to cater to an expanding user base. To meet these demands, the use of the millimeter-wave (MMW) spectrum emerges as a promising solution that can substantially enhance the data rates and capacity of 5G networks [1–3]. Several MMW frequency bands, such as 28 GHz, 38 GHz, and 60 GHz, are being considered for deployment in 5G wireless communications [4]. The 28 GHz band, which exhibits significant performance enhancement over the 4G low frequencies, is becoming the subject of extensive research on 5G networks [5]. Nevertheless, the MMW band experiences a high path loss and interference when contrasted with sub-6 GHz frequencies [6]. Furthermore, vegetation and penetration losses become significant considerations when working in the MMW band [7]. Antennas with a high gain are instrumental in mitigating path loss, while simultaneously, there is a growing demand for dual/multi-beam antennas to effectively combat the challenges posed by multipath fading and interference effects [8,9]. Several methods have been reported in the scientific literature to increase the gain of antennas. These approaches include the use of multiple substrates [10], dielectric resonator antennas (DRAs) [11], and artificial materials [12,13].

Recently, there has been an evident focus in the literature on high-gain antenna arrays utilizing substrate-integrated waveguide (SIW) and microstrip methods [14–19]. In [15], the authors introduced a 1 × 8 Vivaldi antenna array, achieving a gain ranging from 6.96 dBi to 11.3 dBi over a frequency range of 24.75–28.35 GHz. Another design involved a 1 × 8 dipole antenna array, as presented in [16], aiming to enhance the gain to 8 dBi at 18 GHz. The authors of [17] used a 1 × 8 dipole antenna array designed to elevate the gain to 12 dBi at 26 GHz. A 1 × 4 microstrip antenna array was proposed in [18] to achieve a gain of 14 dBi at 31 GHz for satellite communication in the MMW spectrum. However, these designs are large in size. It is feasible to enhance these attainable gains while keeping the antenna compact. In [19], a 2 × 2 dielectric resonator antenna (DRA) array was introduced for 5G applications, featuring a moderate gain of 6.7 dBi at 28 GHz, along with a complex feeding network. Furthermore, the series-fed technique has been reported in recent literature as a means of enhancing antenna gain performance [20–24]. In [20], the authors proposed an eight-element dipole array that attained a peak gain of 10.9 dBi at 28 GHz. Nevertheless, it is essential to highlight that employing eight elements leads to a substantial increase in the overall size. The authors of [21] proposed a series-fed antenna with microstrip-to-grounded co-planar waveguide (CPW) transition to achieve a peak gain of 10.3 dBi in the range of 27.25–28.5 GHz. Yet, with dimensions of 25 × 67 × 0.5 mm^3, the antenna is considered bulky when operating in the high-frequency range. An eight-element series-fed dipole was introduced to reach a maximumgain of 12.3 dBi in the range of 21.1–27.82 GHz [22]. However, the antenna's substantial size, measuring 10 × 59 × 0.203 mm^3, remained a notable factor, despite its good gain performance. A series-fed antenna with four elements was introduced in [23] to increase the gain by up to 11.8 dBi at 27.68 GHz. This performance was achieved with a physical size of 21 × 40 × 1.6 mm^3. The four-element dipole array presented in [24] achieved a wide bandwidth of 1.81–3.78 GHz and a peak gain of 6.78 dBi. The antenna's physical size of 64 × 105 × 1.587 mm^3 is considerably large, alongside its low gain.

High gain is often attained through the use of high-profile structures or antenna arrays, as the gain is directly linked to the antenna's aperture size. Nonetheless, there is an increasing need for compact devices with smaller physical footprints, posing a challenge when it comes to enhancing gain. In the last decade, metamaterials (MMs) have emerged as a cost-effective means of boosting gain without significantly enlarging the antenna's physical dimensions [25]. MMs represent a remarkable category of artificial materials characterized by unique properties not found in natural materials. The integration of these composite structures into various antennas has the potential to substantially enhance their gain performance [26–28]. In [26], the authors employed seven layers of MMs, including six air gaps above the patch antenna, to achieve an impressive gain of 13.7 dBi at 28 GHz. Similarly, the authors of [27] presented a single layer of various MM structures placed above the patch antenna, leading to a peak gain of 11.59 dBi at 28 GHz. However, the inclusion of MM layers leads to an increase in both the size and complexity of the design, forming a 3D structure. The authors of [28] proposed an MM-based dual bow-tie antenna to operate at the mm-wave spectrum with a maximum gain of 12.2 dBi at 29 GHz.

Based on the aforementioned studies, none of the discussed antennas incorporate series-fed antennas with MMs to achieve a high gain in the MMW spectrum. This paper addresses the design and implementation of a high-gain antenna for broadband MMW applications. Three design steps were employed to improve the antenna performance. The first stage involves designing an SIW-based power splitter, followed by the incorporation of the dual dipole antenna to extend the bandwidth from 1.7 GHz (SIW-based power splitter alone) to 4.4 GHz (SIW-based power splitter + dual dipoles). The introduction of series-fed four-dipole antennas further broadens the bandwidth to 7.85 GHz. Additionally, the gain reaches a peak of 10.5 dBi at 30.5 GHz. In the final stage, an MM is designed and integrated with the series-fed antenna to further enhance the gain, resulting in a maximum gain of 14.1 dBi within the operational bandwidth. The contributions of this study are summarized as follows:

I The implementation of a power splitter at 27.5 GHz through the application of substrate-integrated waveguide (SIW);
II Designing a compact four-element series-fed dipole antenna and integrating it with a power splitter to achieve a high gain, reaching a maximum of 10.5 dBi, along with a broad bandwidth spanning from 26.9 GHz to 34.75 GHz.
III Designing an MM structure operating within the MMW spectrum and integrating it with the series-fed antenna to further increase the gain to 14.1 dBi within the operational bandwidth.

In comparison to the latest advancements highlighted in the literature, the suggested design presents a system that is characterized by its low profile and reduced complexity, while still offering a high gain and a wide bandwidth.

2. SIW-Based Series-Fed Dipole

A wide bandwidth plays a crucial role in enabling high data rates for potential 5G applications. The first stage of this manuscript outlines the development of an SIW-based series-fed antenna, designed to achieve a wide bandwidth and high gain for 5G applications in the MMW spectrum. Figure 1a,b display the SIW-based power splitter, comprising an SIW, along with three microstrip lines, that feature one input and two outputs. The power divider's symmetry along the y-axis enables it to uniformly split the input power (P_1) between the two output channels (P_2 and P_3). The divider is constructed using a Rogers substrate with a 0.508 mm thickness and a dielectric constant of ϵ_r = 2.2. The coplanar waveguide facilitates the transfer of power from the microstrip line to the SIW. Circular metallic vias connect the upper and lower metallic layers, as illustrated in Figure 1b. The SIW's resonant frequency can be evaluated as follows [29]:

$$f_{SIW} = \frac{c}{2\sqrt{\varepsilon_r}}\sqrt{\left(\frac{1}{L_{eff}}\right)^2 + \left(\frac{1}{W_{eff}}\right)^2} \quad (1)$$

where

$$L_{eff} = L_s - \frac{d^2}{0.95s} \text{ and, } W_{eff} = W_s - \frac{d^2}{0.95s} \quad (2)$$

Here, L_{eff} and W_{eff} represent the effective length and width of the SIW, with ε_r being the dielectric constant of the substrate. The parameter d refers to the diameter of the via hole, whereas s represents the spacing between the vias. The spacing between vias, s, is less than twice the via diameter, $2d$ (refer to Table 1 for a summary of the symbols used in this paper). The S-parameters of the developed splitter are depicted in Figure 1c. They function effectively at 27.5 GHz and exhibit an impedance bandwidth from 26.9 to 28.6 GHz. The transmission responses, represented by S_{21} and S_{31}, remain consistent across the entire frequency band. This consistency indicates that the input power, P_1, can be evenly distributed between the two outputs, P_2 and P_3. Additionally, at 27.5 GHz, the coefficients S_{21} and S_{31} measure approximately 3.22 dB, resulting in a notably low insertion loss of only 0.22 dB within the MMW spectrum. Figure 2a displays the dual dipole antenna constructed on a power divider. To create this structure, modifications are made to the full ground of the power splitter, as depicted in Figure 1a. This involves cutting along the x-axis and extending two microstrip lines that run parallel to the port lines, P_1 and P_2. In this modified arrangement, the upper and lower metallic layers share the same length along the x-axis. Subsequently, perpendicular to the two ports, two arms are constructed on both the front and back sides with a length of d_1 to accommodate the dipoles along the y-axis. The dipole is inclined at 30°, and this orientation enables a reduction in the antenna's size. Moreover, such antennas demonstrate superior radiation characteristics when compared to their straight-dipole counterparts [20,30]. By adopting this setup, a second-order resonance is introduced at the input, resulting in an extended impedance bandwidth for the dipole antenna and the presence of two reflection zeros around 28 and 30 GHz, as depicted in Figure 3. The CST 2019 software is

employed for simulating antenna configurations. Compared to the power divider, the bandwidth is improved from 1.7 GHz (as seen in Figure 1b) to 4.4 GHz, covering the range of 26.9–31.3 GHz. The single dipole attains a maximum gain of 6.18 dBi within the desired range as shown in Figure 4, which is considered relatively low for MMW communications. To boost the gain and further extend the impedance bandwidth, the proposed setup incorporates a series-fed dipole configuration, as depicted in Figure 2b. In this arrangement, four dipole elements are connected in series and oriented perpendicular to the two ports of the divider. The electromagnetic wave transmitted to the microstrip line was conveyed to the dipole using a parallel stripline printed on both sides of the substrate. In this particular design, a meticulous optimization of the dipole lengths (S_2 through S_4) and spacings (d_2 through d_4) was carried out in CST to achieve the desired outcomes. The values of d_1 and S_1 belong to the original single dipole and are fixed at 5 mm and 2.4 mm, respectively. The spacing values (d_2 = 2.4 mm, d_3 = 2.2 mm, and d_4 = 1.9 mm) and dipole lengths (S_2 = 2 mm, S_3 = 1.6 mm, and S_4 = 1.2 mm) were selected for their superior performance in achieving a broad bandwidth and high gain. Figure 3 illustrates the antenna's reflection coefficient. The findings indicate that by employing four dipole elements and carefully adjusting their lengths and spacing, the impedance bandwidth was enhanced from 4.4 GHz (26.9–31.3 GHz) to 7.85 GHz (26.9–34.75 GHz), rendering it well-suited for coverage in the 5G band at 28 GHz. The addition of copper strips of length a_l and width a_w to the dipole arms serves to enhance the reflection magnitude. In Figure 4, the simulated gain curves of the single and series-fed antennas are depicted. It is evident that the series-fed antenna demonstrates significantly improved gain across the entire operating band when compared to the dual dipole antenna. At 30.5 GHz, the gain reaches a maximum of 10.5 dBi. Figure 5 exhibits the radiation patterns in both the E-plane and H-plane for the series-fed antenna at 28 GHz. The input signal is uniformly split between the two branches of the series-fed antenna. This equal distribution results in dual-beam radiation in the E-plane at $\pm 20^\circ$ (co-polarization), which represents a significant advantage of the proposed antenna. The series-fed antenna provides low cross-polarization in the end-fire direction and remains below -22 dB when scanning to $\pm 20^\circ$ in both the E- and H-planes.

Table 1. The symbols employed in this paper.

Symbol	Description
f_{SIW}	SIW's resonant frequency
L_{eff}	Effective length of the SIW
W_{eff}	Effective width of the SIW
L_S	Length of the SIW
W_S	Width of the SIW
ε_r	Dielectric constant of the substrate
d	Diameter of the via hole
s	The spacing between the vias
c	Speed of light
n	Refractive index
z	Impedance
k_o	Wavenumber
t	Thickness of the MM structure
img	Imaginary component of the complex number
Re	Real component of the complex number
m	Branch index of n

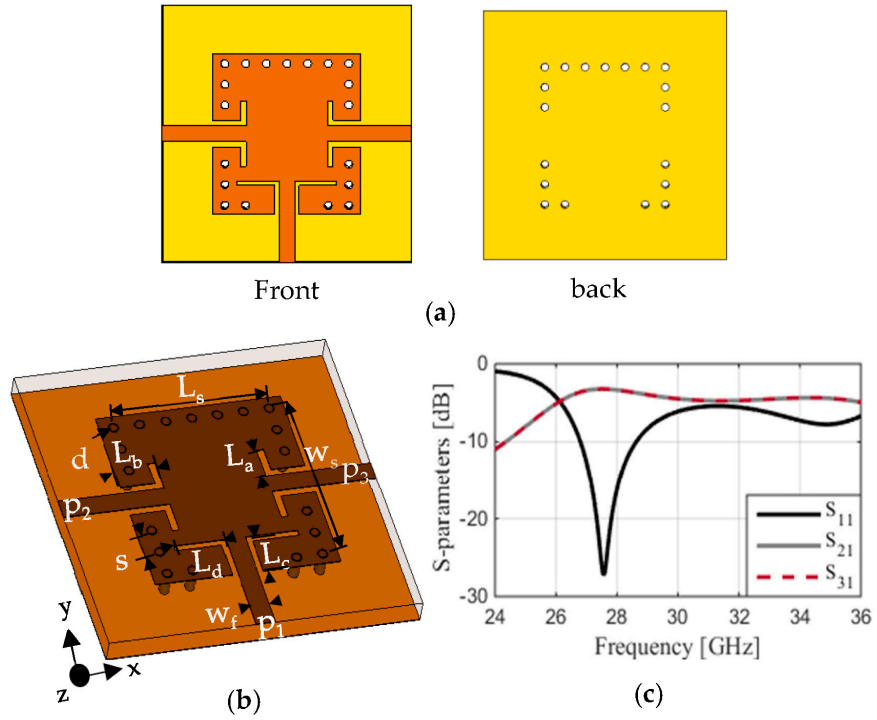

Figure 1. The configuration of the SIW power splitter and its performance: (**a**) front and back views, (**b**) geometrical configuration—dimensions in mm: L_a = 5, W_a = 5.2, L_a = 0.81, L_b = 1.1, L_c = 1.2, L_d = 1.35, s = 0.68, d = 0.32, w_f = 0.5—and (**c**) the *S*-parameters.

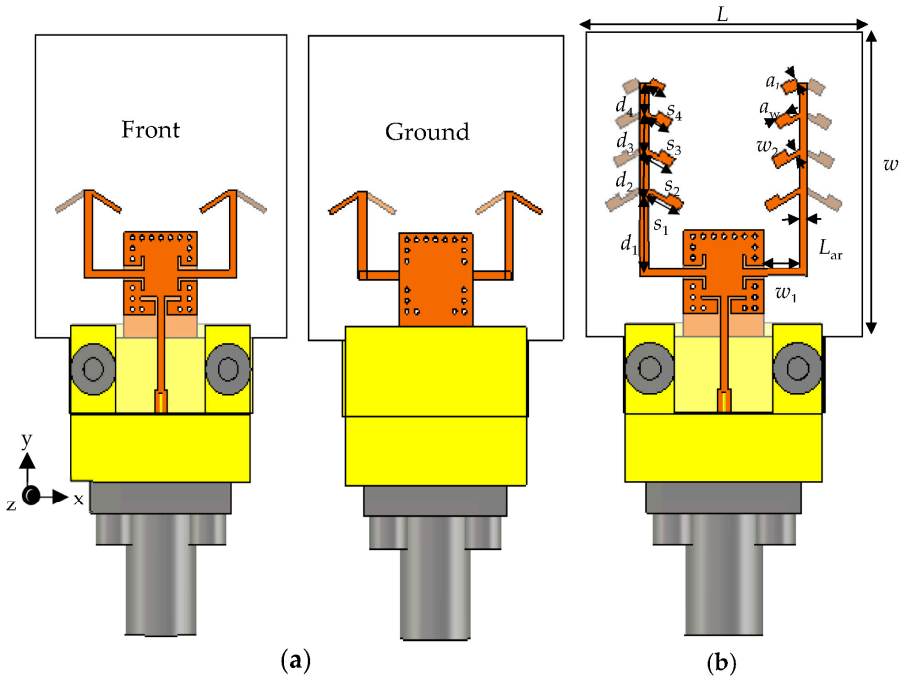

Figure 2. The antenna configuration: (**a**) the front and back views of the dual dipole antenna and (**b**) the proposed series-fed antenna configuration—dimensions in mm: L = 18.7, w = 19, w_1 = 2.1, s_1 = 2.4, s_2 = 2, s_3 = 1.6, s_4 = 1.2, d_1 = 5, d_2 = 2.4, d_3 = 2.2, d_4 = 1.9, a_l = 0.65, a_w = 1, w_2 = 0.3, L_{ar} = 0.5.

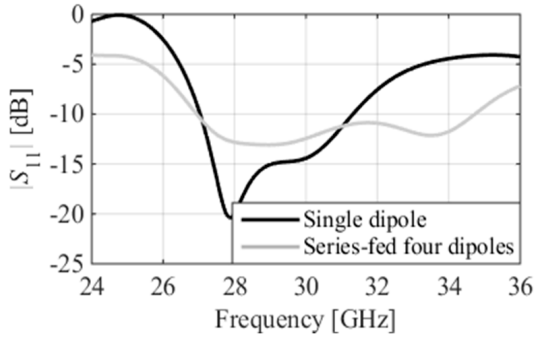

Figure 3. Reflection coefficients of the single-dipole and series-fed four-dipole antennas.

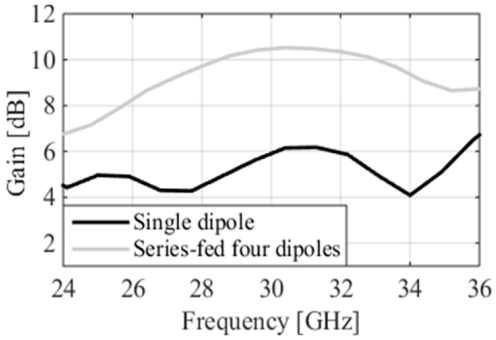

Figure 4. The gain curves of the single dipole and series-fed four-dipole antennas.

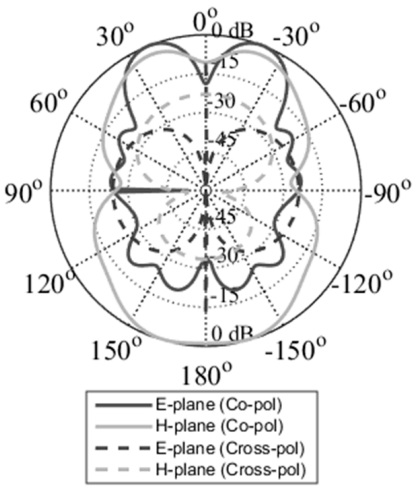

Figure 5. The E- and H-plane radiation patterns of the series-fed antenna at 28 GHz.

3. MM-Inspired High-Gain Antenna

The gain performance of the dual series-fed antenna is improved by integrating an array of modified H-shaped resonators on the front side of the substrate. Figure 6 illustrates the arrangement of the dual series-fed antenna integrated with the MM array. An arrangement of 11 × 6 MM unit cells were placed in front of the antenna, while 9 × 1 unit cells were positioned adjacent to the two branches of the four dipoles. The number of MM unit cells was optimized through a simulation to achieve a high gain while maintaining a reasonable physical size. Due to substrate length limitations, there are six unit cells along the *x*-axis. The MM rows along the *y*-axis were increased to achieve the desired gain, while still maintaining an acceptable physical size. Specifically, they are fixed at eleven above the series-fed antenna, resulting in a maximum gain of 14.1 dBi. Notably, the central section of

the substrate was intentionally left without loading MMs to prevent any impact on the impedance bandwidth. The MM unit cell configuration and geometric specifications are displayed in Figure 7a, featuring a modified version of the H-shaped resonator. The Rogers substrate, with the same thickness of 0.508 mm, is employed, just as in the antenna design. Assigning boundary conditions to all sides of the unit cell is essential to understand the structure's behavior. The perfect electric conductor boundary is positioned along the x-direction, and the perfect magnetic conductor is implemented along the z-direction, whereas the y-axis serves as the route for normally incident electromagnetic waves. The selection of the y-axis for exciting the MM structure is driven by the fact that the antenna serves as the source of the electromagnetic wave propagating through the MMs along the y-direction. This aligns with the MM propagating mode, as previously explained. The MM response is depicted in Figure 7b, showcasing the operation of the structure at 25.7 GHz. The robust retrieval method, as described in [31], is utilized for reconstructing the refractive index of the proposed MM structure. This method is capable of calculating the refractive index, n, and the impedance, z, from the reflection and transmission coefficients. The complex S-parameters are related to n and z as follows:

$$S_{11} = \frac{R_z\left(1 - e^{i2nk_o t}\right)}{1 - {R_z}^2 e^{i2nk_o t}} \tag{3}$$

$$S_{21} = \frac{\left(1 - {R_z}^2\right)e^{i2nk_o d}}{1 - {R_z}^2 e^{i2nk_o d}} \tag{4}$$

where $R_z = z - 1/z + 1$. By reversing (2) and (3), z can be expressed as

$$z = \sqrt{\frac{(1 + S_{11})^2 - {S_{21}}^2}{(1 - S_{11})^2 - {S_{21}}^2}} \tag{5}$$

The refractive index is given by

$$n = \frac{1}{kd}\left[\left\{img\left[\ln\left(e^{ink_o t}\right)\right] + 2m\pi\right\} - i\,Re\left[\ln\left(e^{ink_o t}\right)\right]\right] \tag{6}$$

and

$$e^{ink_o d} = \frac{S_{21}}{1 - S_{11}R_z} \tag{7}$$

where k_o (t) is the wavenumber (thickness) of the MM structure, and the img (Re) represents the imaginary (real) component of the complex number. m is the branch index of n. Table 1 presents the symbols employed in this paper. In Figure 7c, the refractive index of the modified H-shaped structure is displayed, revealing an almost zero refractive index within the desired frequency range. This remarkable feature, zero refractive index, can be leveraged to increase gain when combined with antennas. Gain enhancement can be explained using Snell's law of refraction, which is expressed as

$$sin\theta i \cdot n_i = sin\theta r \cdot n_r \tag{8}$$

where n_i and n_r denote the refractive indices of the incident and refracted rays, respectively, and θ_i and θr stand for the angles of the incident and refracted rays. Figure 7d depicts the wave propagation in both MM and air. In this context, as the incident rays transition from a medium with a refractive index of zero ($n_\mathrm{i} = n_\mathrm{MM} = 0$) to a high refractive index medium

($n_r = n_{air} = 1$), the refracted rays disperse along a path that is normal to the interface. Consequently, the phase change in the electromagnetic wave is close to or equals zero, resulting in an increase in gain in the direction of emission. The equivalent circuit of the proposed series-fed antenna-loading MMs is displayed in Figure 8. L_{in} and C_{in} are utilized to model the system feed. The series inductor L_v and parallel elements L_s and C_s are employed to model the SIW [32,33]. An equivalent circuit of a microstrip patch, comprising a parallel inductor (L_d) and capacitor (C_d), is employed to model the series dipoles, as elucidated in [34]. A coupling capacitor (C_1) is integrated between dipoles connected in parallel with SIW to facilitate electromagnetic coupling. The H-shaped resonator is characterized by capacitance C_h, symbolizing the gap at the middle of the structure, while L_h and L_{h1} represent the copper strips on both sides of the unit cell [35]. The equivalent circuit of the set of 11 × 6 unit cells, in front of the dipoles, is presented and connected to the dipoles via capacitance C_2. C_3 connects the left three rows to the right ones, and C_5 establishes connections between each unit cell. Furthermore, an equivalent circuit of the set of 9 × 1 unit cells, positioned adjacent to the two branches of the dipoles, is presented and connected to the dipoles via capacitance C_4. The reflection coefficient and gain plots of the series-fed antenna loading MMs are presented in Figure 9a,b, respectively. The inclusion of the MM minimally affects the impedance-matching performance of the MM antenna in comparison to the unloaded antenna, cf. Figures 3 and 9a. It is noticeable that the presence of MMs influences the reflection amplitude, but the bandwidth remains almost unchanged. Before incorporating the MMs, the series-fed antenna exhibits a significantly improved gain, reaching a maximum of 10.5 dBi at 30.5 GHz, as illustrated in Figure 4. Nevertheless, upon integrating the metamaterial with a refractive index of zero response within the operational bandwidth, the gain is further enhanced, reaching a maximum of 14.1 dBi, as seen in Figure 9b. The co and cross-polarization radiation patterns in the E- and H-planes for the series-fed antenna based on MMs at 28 GHz are depicted in Figure 10. It can be observed that the developed MM antenna provides a low co-polarization, especially in the E-plane. The cross-polarization is slightly higher in the H-plane compared to that of the unloaded series-fed antenna (Figure 5). This can be attributed to the inclusion of MMs. The input signal is evenly divided between the two branches of the series-fed antenna. This equitable distribution leads to radiation with a dual-beam property in the E-plane, which is a notable advantage of the proposed antenna, as illustrated in Figure 8. Employing dual-beam radiation at both transmitter and receiver leads to considerable enhancement of the link quality when an obstacle blocks the link [36]. Furthermore, it assists in addressing multipath fading and interference effects [8,9].

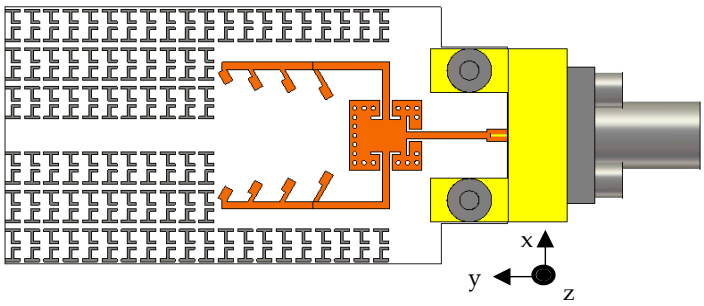

Figure 6. The proposed series-fed antenna configuration with MM loading.

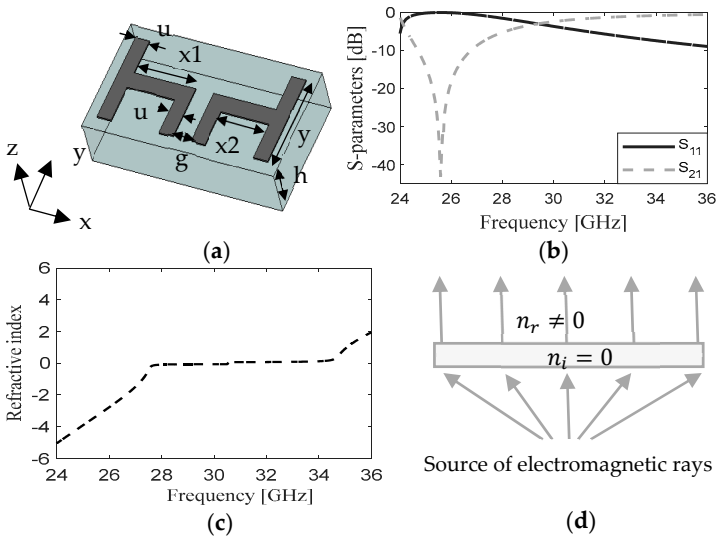

Figure 7. Geometric specifications of the proposed MM unit cell and its performance: (**a**) the configuration (dimensions: y = 1.1 mm, u = 0.2 mm, x_1 = 0.875 mm, x_2 = 0.675 mm, g = 0.25 mm, h = 0.508 mm), (**b**) S-parameters, (**c**) refractive index, and (**d**) the electromagnetic wave propagation based on the zero index layer.

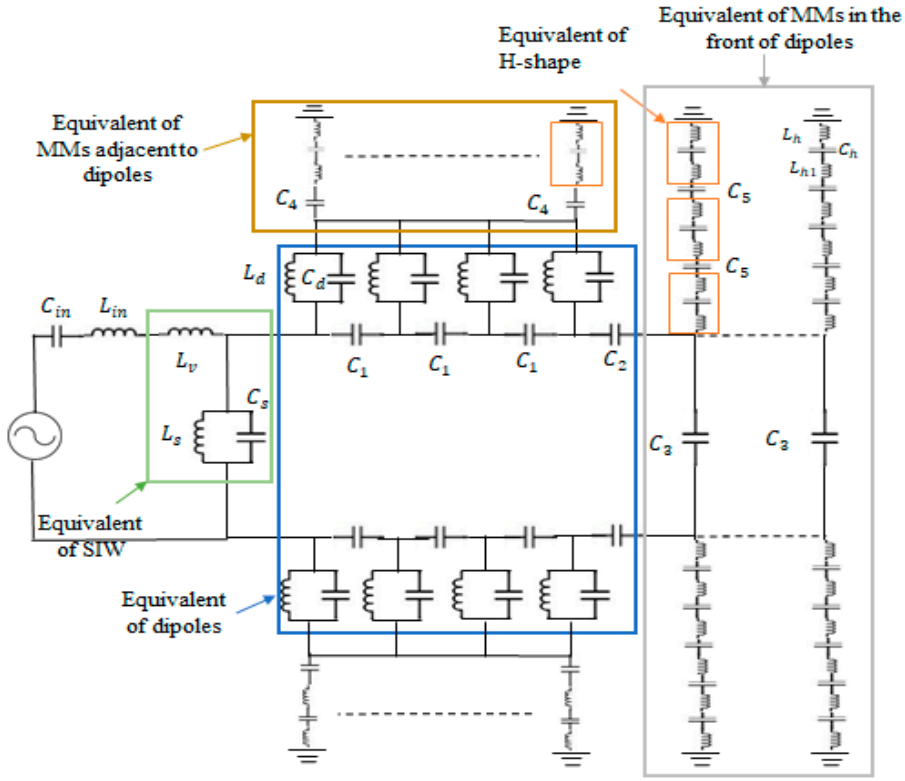

Figure 8. The equivalent circuit of the series-fed antenna loading MMs.

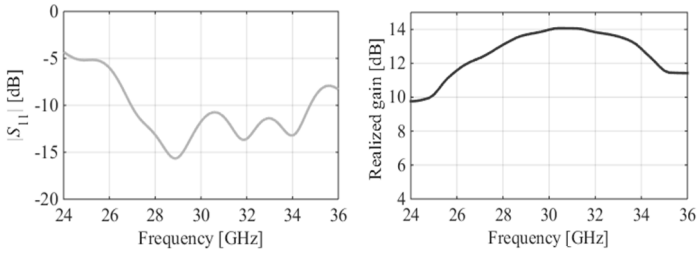

Figure 9. The performance of the series-fed antenna with MM loading: (**a**) the reflection coefficient and (**b**) the gain.

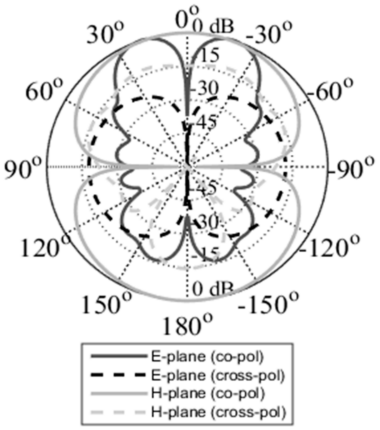

Figure 10. The co- and cross-polarization of the E- and H-planes radiation patterns at 28 GHz.

4. Results

The series-fed antenna integrated with MMs is manufactured to verify the simulation results and demonstrate its suitability for 5G MMW applications. Figure 11 displays both the front and rear views of the fabricated antenna. The measurements were performed using an Anritsu vector network analyzer MS4644B (0–40 GHz), whereas the validation of radiation patterns took place in an anechoic chamber, as seen in Figure 12. The comparison of $|S_{11}|$ between the simulated and measured data is depicted in Figure 13. The antenna achieved a wide impedance bandwidth ranging from 26.9 to 34.75 GHz, effectively covering the 28 GHz 5G band. A reasonable agreement can be observed between both datasets for $|S_{11}|$. Nevertheless, a minor difference in the resonant magnitude was observed when comparing the measured and simulated data. This variation may be attributed to various factors, including inaccuracies pertaining to manufacturing, cable losses, assembly flaws, and the use of a bulky end-launch connector. Figure 14 depicts the gain plots of the developed series-fed antenna, offering a comparison between the simulated and measured outcomes. Within the desired frequency range of 26.9–34.75 GHz, the simulated gain extends from 12 to 14.1 dBi. The measurement data closely align with the simulation results across the entire band, exhibiting only a slight deviation at 28.5 GHz and 34 GHz. This discrepancy may be explained as previously by inaccuracies pertaining to manufacturing, the other reasons may include imprecise assembly of the antenna or inaccurate angular placement of the antenna in the chamber. The radiation patterns in the E-plane and H-plane for the series-fed antenna integrated with MMs at 27 GHz, 28 GHz and 32 GHz are illustrated in Figure 15a–c, respectively. In the E-plane pattern, a dual-beam feature at $\pm 20^{\circ}$ (co-polarization) aligns with the simulation-based predictions. The design provides low cross-polarization in the end-fire direction and remains below -22 dB when scanning to $\pm 20^{\circ}$ in the E-plane at the three frequencies. The cross-polarization is slightly higher in the H-plane when compared to that of the unloaded series-fed antenna. This can be attributed to the incorporation of MMs. A comparison of the measured radiation patterns with simulation results reveals good agreement in both the E-plane and H-plane for the three

frequencies, with a minor discrepancy observed in the H-plane pattern. This discrepancy is likely attributable to the same factors mentioned earlier, such as inaccuracies pertaining to manufacturing, as well as the sensitivity of measurements in the high-frequency range. The proposed design has been compared to several state-of-the-art antennas reported in the literature, all operating in comparable frequency ranges. Numerical data can be found in Table 2. The comparison includes details on antenna type, physical size, substrate used, operating frequency, gain and method employed to achieve it, and the aperture efficiency. It is clear that the antenna presented in this study outperforms the benchmark structures with respect to essentially all performance indicators. It offers considerably higher gain while being physically smaller by a large margin. With an aperture efficiency of 36%, the design outshines all references in Table 2, except for reference [26]. Yet, across all other performance metrics, the MM antenna developed in this study outperforms reference [26]. On the other hand, the design is geometrically simple and straightforward to manufacture within the standard PCB technology.

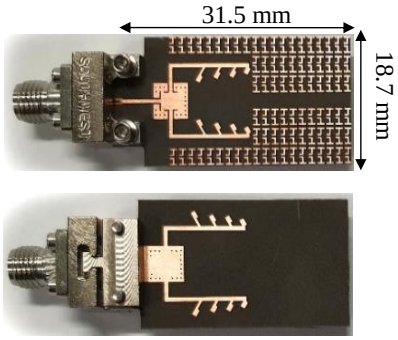

Figure 11. The fabricated MM-based series-fed SIW antenna.

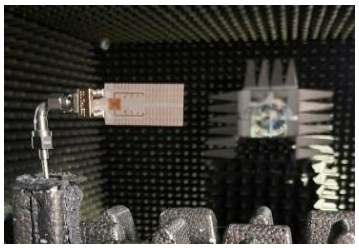

Figure 12. The radiation pattern measurement setup.

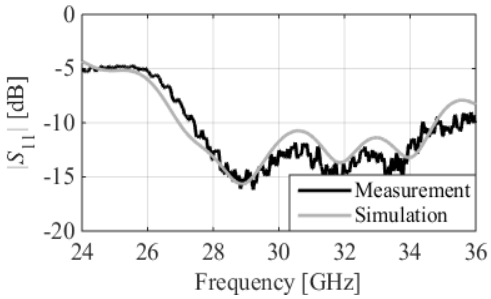

Figure 13. Simulated and measured reflection coefficient.

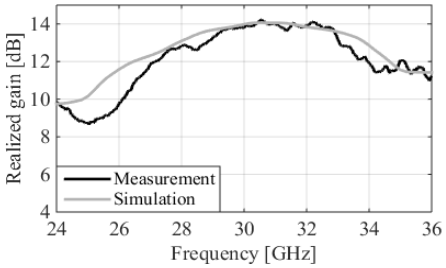

Figure 14. Simulated and measured antenna gain.

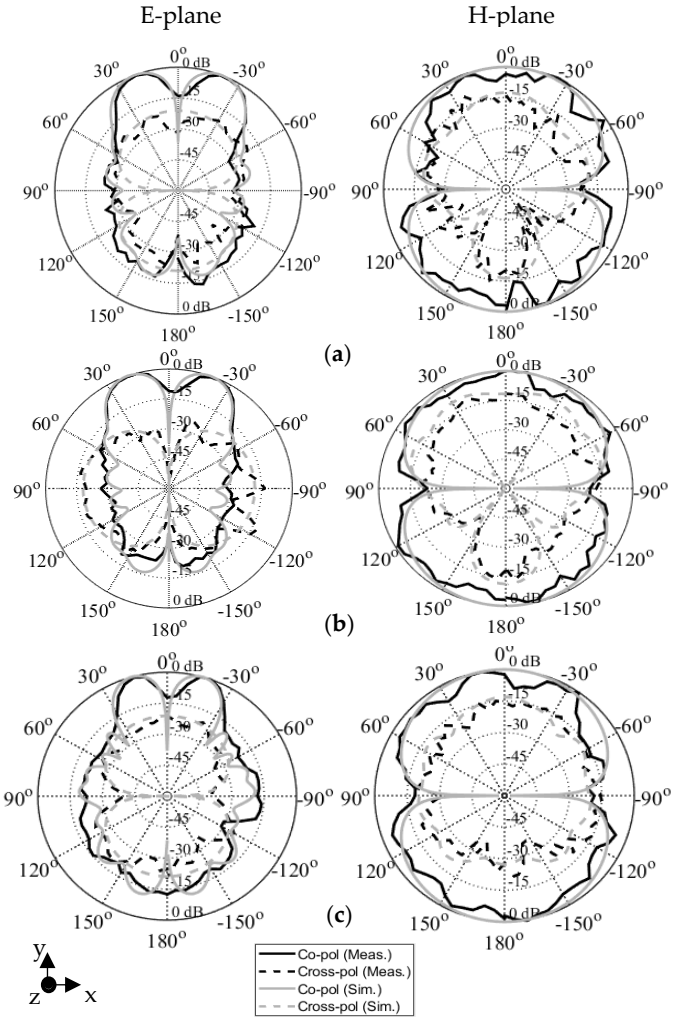

Figure 15. The E- and H-plane radiation patterns of the series-fed antenna integrated MMs at (**a**) 27 GHz, (**b**) 28 GHz, and (**c**) 32 GHz.

Table 2. Comparison of the proposed antenna with state-of-the-art structures.

Ref.	Antenna Structure (Size mm^3)	Substrate (ε_r)	Frequency (GHz)	Max. Gain (dB)	Aperture Efficiency (%)	Method
[15]	Vivaldi antenna (28.82 × 60 × 0.787)	Rogers RT 5880 (2.2)	25.5	11.3	8.58	1 × 8 array
[16]	Dipole antenna (112 × 50 × 3)	Taconic-TLY (2.2)	18	8	2.5	1 × 8 array
[17]	Dipole antenna (66 × 15 × 0.3)	Rogers RT 5880 (2.2)	26	11	13.4	1 × 8 array

Table 2. *Cont.*

Ref.	Antenna Structure (Size mm^3)	Substrate (ε_r)	Frequency (GHz)	Max. Gain (dB)	Aperture Efficiency (%)	Method
[18]	Patch (13.4 × 50.8 × 0.508)	Rogers RT 5880 (2.2)	31	14	27.4	1 × 4 array
[19]	DRA (20.7 × 21.2 × 1.5)	Rogers RT/duroid 6010.2LM (2.2)	28	6.7	9.7	2 × 2 array on substrates of three layers
[20]	Dipole (10 × 36.5 × 0.2032)	RO4003C (3.38)	28	10.9	30.7	Series-fed eight-element dipole
[21]	Dipole (25 × 67 × 0.5)	RO5880 (2.2)	28.5	10.3	5.6	Series-fed six-element dipole
[22]	Dipole (10 × 59 × 0.203)	RO4003C (3.55)	28	12.3	26.2	Series-fed eight-element dipole
[23]	Patch (21 × 40.8 × 1.6)	Rogers RT 5880 (2.2)	27.68	11.8	16.8	Series-fed four-element patch
[26]	Patch (14.7 × 28 × 7)	Rogers 5870 (2.2)	28	12.6	40.2	Seven MM layers (3D structure)
[27]	Microstrip (18 × 22 × 16)	RO4003 (3.38)	28	11.59	33.1	One MM layer (3D structure)
This study	Dipole (31.5 × 18.7 × 0.508)	Rogers RT 5880 (2.2)	30.5	14.1	36	Series-fed + Etching the MMs on the antenna substrate

5. Conclusions

A broadband and high-gain series-fed antenna based on SIW was presented, which covers the 5G communication frequency band of 27.5–28.35 GHz. Four dipoles were installed on each port of the SIW-based power splitter. The power splitter operated at 27.5 GHz with an impedance bandwidth of 26.9–28.6 GHz, which was extended to 26.9–34.75 GHz by including the four dipoles. Furthermore, the gain was improved from 6.18 dBi (dual dipoles) to 10.5 dBi (series-fed four dipoles). To further enhance the performance without significantly increasing the size, an MM array was integrated onto the front side of the antenna substrate. Consequently, the proposed antenna achieved a maximum gain of 14.1 dBi at 30.5 GHz, demonstrating a significant gain improvement compared to the original series-fed antenna. Furthermore, the MM-based series-fed antenna exhibits symmetrical dual-beam E-plane radiation at $\pm 20^\circ$ at 28 GHz in the end-fire direction. The developed system underwent experimental validation, demonstrating outstanding agreement between the simulated and measured data. When compared to the state-of-the-art advancements reported in the literature, this design provides a low-profile, simplified system while delivering a high gain and wide bandwidth.

Author Contributions: Conceptualization, methodology, and CST 2019 software, B.A.F.E.; validation, S.K.; formal analysis and investigation, B.A.F.E. and D.I.; resources, S.K.; writing—original draft preparation, B.A.F.E.; writing—review and editing, S.K. and D.I.; supervision, S.K. and D.I.; project administration, S.K.; funding acquisition, D.I. All authors have read and agreed to the published version of the manuscript.

Funding: This research was supported in part by the Natural Sciences and Engineering Research Council of Canada (NSERC) Discovery Grant program grant number RGPIN-2017-04974.

Data Availability Statement: Data are contained within the article.

Conflicts of Interest: The authors declare no conflict of interest.

References

1. Askari, H.; Hussain, N.; Sufian, M.A.; Lee, S.M.; Kim, N. A Wideband Circularly Polarized Magnetoelectric Dipole Antenna for 5G Millimeter-Wave Communications. *Sensors* **2022**, *22*, 2338. [CrossRef]
2. Ouamri, M.A.; Oteşteanu, M.E.; Isar, A.; Azni, M. Coverage, Handoff and cost optimization for 5G Heterogeneous Network. *Phys. Commun.* **2020**, *39*, 101037. [CrossRef]
3. Ouamri, M.A. Stochastic geometry modeling and analysis of downlink coverage and rate in small cell network. *Telecommun. Syst.* **2021**, *77*, 767–779. [CrossRef]
4. Esmail, B.A.F.; Koziel, S. Design and optimization of metamaterial-based dual-band 28/38 GHz 5G MIMO antenna with modified ground for isolation and bandwidth improvement. *IEEE Antennas Wirel. Propag. Lett.* **2023**, *22*, 1069–1073. [CrossRef]
5. Ibrahim, A.A.; Zahra, H.; Dardeer, O.M.; Hussain, N.; Abbas, S.M.; Abdelghany, M.A. Slotted Antenna Array with Enhanced Radiation Characteristics for 5G 28 GHz Communications. *Electronics* **2022**, *11*, 2664. [CrossRef]
6. Zhang, P.; Yang, B.; Yi, C.; Wang, H.; You, X. Measurement-based 5G millimeter-wave propagation characterization in vegetated suburban macrocell environments. *IEEE Trans. Antennas Propag.* **2020**, *68*, 5556–5567. [CrossRef]
7. Barb, G.; Danuti, F.; Ouamri, M.A.; Otesteanu, M. Analysis of Vegetation and Penetration Losses in 5G mmWave Communication Systems. In Proceedings of the 2022 International Symposium on Electronics and Telecommunications (ISETC), Timisoara, Romania, 10–11 November 2022.
8. Hwang, I.-J.; Oh, J.-I.; Jo, H.-W.; Kim, K.-S.; Yu, J.-W.; Lee, D.-J. 28 GHz and 38 GHz Dual-Band Vertically Stacked Dipole Antennas on Flexible Liquid Crystal Polymer Substrates for Millimeter-Wave 5G Cellular Handsets. *IEEE Trans. Antennas Propag.* **2022**, *70*, 3223–3236. [CrossRef]
9. Ding, K.; Leenaerts, D.M.; Gao, H. A 28/38 GHz Dual-Band Power Amplifier for 5G Communication. *IEEE Trans. Microw. Theory Tech.* **2022**, *70*, 4177–4186. [CrossRef]
10. Lugo, D.C.; Ramirez, R.A.; Wang, J.; Weller, T.M. Multilayer dielectric end-fire antenna with enhanced gain. *IEEE Antennas Wirel. Propag. Lett.* **2018**, *17*, 2213–2217. [CrossRef]
11. Liu, H.; Tian, H.; Liu, L.; Feng, L. Co-design of wideband filtering dielectric resonator antenna with high gain. *IEEE Trans. Circuits Syst. II Express Briefs* **2022**, *69*, 1064–1068. [CrossRef]
12. Shi, C.; Zou, J.; Gao, J.; Liu, C. Gain Enhancement of a Dual-Band Antenna with the FSS. *Electronics* **2022**, *11*, 2882. [CrossRef]
13. Esmail, B.A.F.; Majid, H.A.; Dahlan, S.H.; Abidin, Z.Z.; Rahim, M.K.A.; Abdullah, M.A.; Jusoh, M. Antenna beam tilting and gain enhancement using novel metamaterial structure at 28 GHz. In Proceedings of the 2018 IEEE International RF and Microwave Conference (RFM), Penang, Malaysia, 17–19 December 2018.
14. Desai, A.; Tsao, Y.F.; Hsu, H.T. High gain substrate integrated waveguide antenna with enhanced bandwidth for millimeter-wave wireless network applications. *Wirel. Netw.* **2023**, *29*, 2251–2260. [CrossRef]
15. Zhu, S.; Liu, H.; Chen, Z.; Wen, P. A compact gain-enhanced Vivaldi antenna array with suppressed mutual coupling for 5G mmWave application. *IEEE Antennas Wirel. Propag. Lett.* **2018**, *17*, 776–779. [CrossRef]
16. Wang, J.; Zhao, X.; Ye, Y.; Liu, S. A Millimeter-Wave Ultrawideband Tightly Coupled Dipole Array Antenna for Vehicle Communication. *IEEE Antennas Wirel. Propag. Lett.* **2022**, *21*, 2135–2139. [CrossRef]
17. Mao, C.-X.; Khalily, M.; Xiao, P.; Brown, T.W.C.; Gao, S. Planar Sub-Millimeter-Wave Array Antenna with Enhanced Gain and Reduced Sidelobes for 5G Broadcast Applications. *IEEE Trans. Antennas Propag.* **2019**, *67*, 160–168. [CrossRef]
18. Kadiyam, S.; Jhansi Rani, A. Design and Analysis of a High Gain Millimeter-Wave Antenna Array for Dual Purpose Applications. *Wirel. Pers. Commun.* **2023**, *130*, 593–607. [CrossRef]
19. Liu, Y.-T.; Leung, K.W. 28 GHz Substrate-Integrated Filtering Dielectric Resonator Antenna Array. *IEEE Trans. Antennas Propag.* **2022**, *70*, 9900–9905. [CrossRef]
20. Wang, H.; Kedze, K.E.; Park, I. A high-gain and wideband series-fed angled printed dipole array antenna. *IEEE Trans. Antennas Propag.* **2020**, *68*, 5708–5713. [CrossRef]
21. Maurya, N.K.; Ammann, M.J.; Mcevoy, P. Series-fed omnidirectional mm-wave dipole array. *IEEE Trans. Antennas Propag.* **2023**, *71*, 1330–1336. [CrossRef]
22. Liu, Y.; Yagoub, M.C.E. Compact omnidirectional millimeter-wave antenna array fed in series by a novel feed network. *IEEE Trans. Antennas Propag.* **2022**, *69*, 7604–7612. [CrossRef]
23. Duddu, S.K.; Kumar, J. High-Gain Series-Fed-Planar Millimetre-Wave Franklin Antenna Array. *Arab. J. Sci. Eng.* **2023**, 1–11. [CrossRef]
24. Ma, T.; Ai, J.; Shen, M.; Joines, W.T. Design of novel broadband endfire dipole array antennas. *IEEE Antennas Wirel. Propag. Lett.* **2017**, *16*, 2935–2938. [CrossRef]
25. Esmail, B.A.F.; Koziel, S.; Szczepanski, S. Overview of planar antenna loading metamaterials for gain performance enhancement: The two decades of progress. *IEEE Access* **2022**, *10*, 27381–27403. [CrossRef]
26. Wani, Z.; Abegaonkar, M.P.; Koul, S.K. High-low-epsilon biaxial anisotropic lens for enhanced gain and aperture efficiency of a linearly polarized antenna. *IEEE Trans. Antennas Propag.* **2020**, *68*, 8133–8138. [CrossRef]
27. Jeong, M.; Hussain, N.; Abbas, A.; Rhee, S.Y.; Lee, S.M.; Gil, S.-K.; Kim, N. Performance improvement of microstrip patch antenna using a novel double-layer concentric rings metaplate for 5G millimeter wave applications. *Int. J. RF Microw. Comput.-Aided Eng.* **2020**, *31*, e22509. [CrossRef]

28. Esmail, B.A.F.; Koziel, S. Design and Optimization of Metamaterial-Based 5G Millimeter Wave Antenna for Gain Enhancement. *IEEE Trans. Circuits Syst. II Express Briefs* **2023**, *70*, 3348–3352. [CrossRef]
29. Chen, X.P.; Wu, K.; Drolet, D. Substrate integrated waveguide filter with improved stopband performance for satellite ground terminal. *IEEE Trans. Microw. Theory Tech.* **2009**, *57*, 674–683. [CrossRef]
30. Ta, S.X.; Choo, H.; Park, I. Broadband printed-dipole antenna and its arrays for 5G applications. *IEEE Antennas Wirel. Propag. Lett.* **2017**, *16*, 2183–2186. [CrossRef]
31. Chen, X.; Grzegorczyk, T.M.; Wu, B.I.; Pacheco, J., Jr.; Kong, J.A. Robust method to retrieve the constitutive effective parameters of metamaterials. *Phys. Rev. E* **2004**, *70*, 016608. [CrossRef]
32. Li, D.; Wang, J.A.; Yu, Y.; Liu, Y.; Chen, Z.; Yang, L. Substrate integrated waveguide-based complementary split-ring resonator and its arrays for compact dual-wideband bandpass filter design. *Int. J. RF Microw. Comput.-Aided Eng.* **2021**, *31*, e22504. [CrossRef]
33. Zhao, L.; Li, Y.; Chen, Z.M.; Liang, X.H.; Wang, J.; Shen, X.; Zhang, Q. A band-pass filter based on half-mode substrate integrated waveguide and spoof surface plasmon polaritons. *Sci. Rep.* **2019**, *9*, 13429. [CrossRef] [PubMed]
34. Pawar, S.S.; Shandilya, M.; Chaurasia, V. Parametric evaluation of microstrip log periodic dipole array antenna using transmission line equivalent circuit. *Eng. Sci. Technol. Int. J.* **2017**, *20*, 1260–1274. [CrossRef]
35. Esmail, B.A.F.; Majid, H.B.; Dahlan, S.H.; Abidin, Z.Z.; Rahim, M.K.; Jusoh, M. Planar antenna beam deflection using low-loss metamaterial for future 5G applications. *Int. J. RF Microw. Comput.-Aided Eng.* **2019**, *29*, e21867. [CrossRef]
36. Hosoya, K.; Prasad, N.; Ramachandran, K.; Orihashi, N.; Kishimoto, S.; Rangarajan, S.; Maruhashi, K. Multiple sector ID capture (MIDC): A novel beamforming technique for 60-GHz band multi-Gbps WLAN/PAN systems. *IEEE Trans. Antennas Propag.* **2015**, *63*, 81–96. [CrossRef]